Electronic supplementary information

Flower-to-petal structural conversion and enhanced interfacial storage capability of hydrothermally crystallized $MnCO_3$ *via* the *in situ* mixing of graphene oxide

Shiqiang Zhao, Fan Feng, Faqi Yu and Qiang Shen*

Key Laboratory for Colloid and Interface Chemistry of Education Ministry, School of Chemistry and Chemical Engineering, Shandong University, Jinan 250100, PR China (Tel.: +86-531-88361387; fax: +86-531-88564464; e-mail: qshen@sdu.edu.cn.).

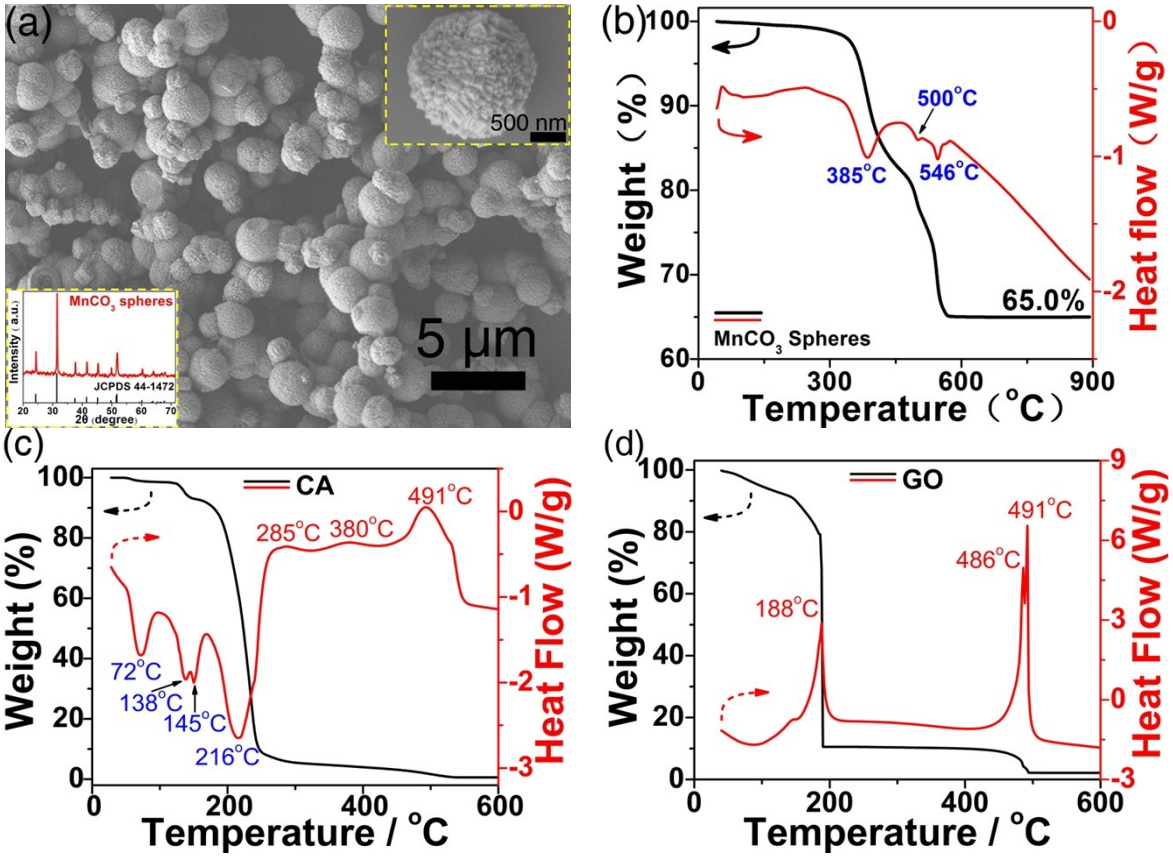

Fig. S1 (a) SEM image, XRD pattern and (b) TGA-DSC curves of $MnCO_3$ spheres prepared in the absence of citric acid monohydrate (CA) and GO. (c, d) TGA-DSC curves of as-supplied citric acid monohydrate (CA) and as-prepared graphene oxide (GO) performed at a heating rate of 10 °C min^{-1} from room temperature to 900 °C under air atmosphere, respectively.

As for the 15-h hydrothermal reaction of manganese acetate $Mn(CH_3COO)_2$ with equimolar

ammonium bicarbonate NH_4HCO_3 at 160°C, the absence of additive CA and GO induces the precipitation of $MnCO_3$ microspheres (Fig. S1-a), while the presence of additive CA causes the unique formation of $MnCO_3$ flower-like hierarchical structures composed of nanospindles (Fig. 1a).

The thermal behavior of phase-pure $MnCO_3$ (Fig.S1-b) presents three endothermic peaks at 385, 500 and 546 °C, which correspond to the decomposition of $MnCO_3$ to Mn_2O_3 under air atmosphere. The comparison of Fig.S1 with Fig.1 indicates that: (i) a strong electrostatic interaction between the R-COO^- head-groups of CA and Mn^{2+} ions may determine the oriented attachment of tiny build blocks and then explains the formation of secondary nanospindles or flowerlike hierarchical structures; (ii) the further addition of GO exerts few influences on the crystallization and initial aggregation of nanocrystalline $MnCO_3$ but greatly impedes the subsequent aggregation of secondary nanospindles into flowerlike hierarchical structures.

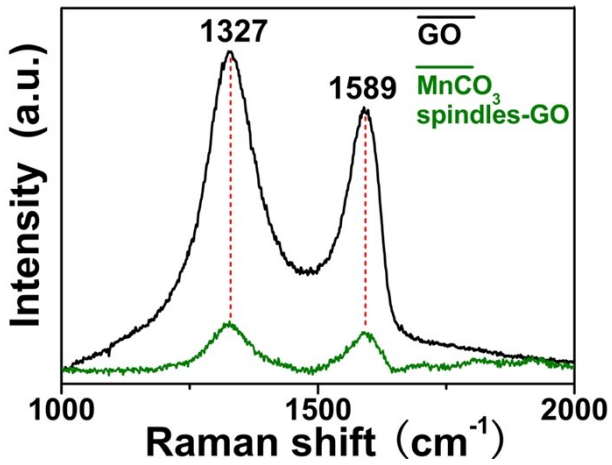

Fig. S2 Raman spectra of $MnCO_3$ spindles-GO composite (green line) and GO (black line).

Raman spectra were collected on a HR800 spectrometer (λ = 473 nm) within the wavenumber range of 1000 and 2000 cm^{-1}. It should be mentioned that, by comparison, the relatively low Raman peak intensities of GO in the $MnCO_3$ spindles-GO composites is due to its relatively small weight fraction therein.

The similar Raman characteristics and the nearly same D-to-G band peak intensity ratios (i.e., the I_D/I_G ratios), together with the absence of GO XRD characteristics for the $MnCO_3$ spindles-GO composites, indicate that both $MnCO_3$ nanospindles and hydrophilic GO may be homogeneously dispersed under the previous suspension condition.

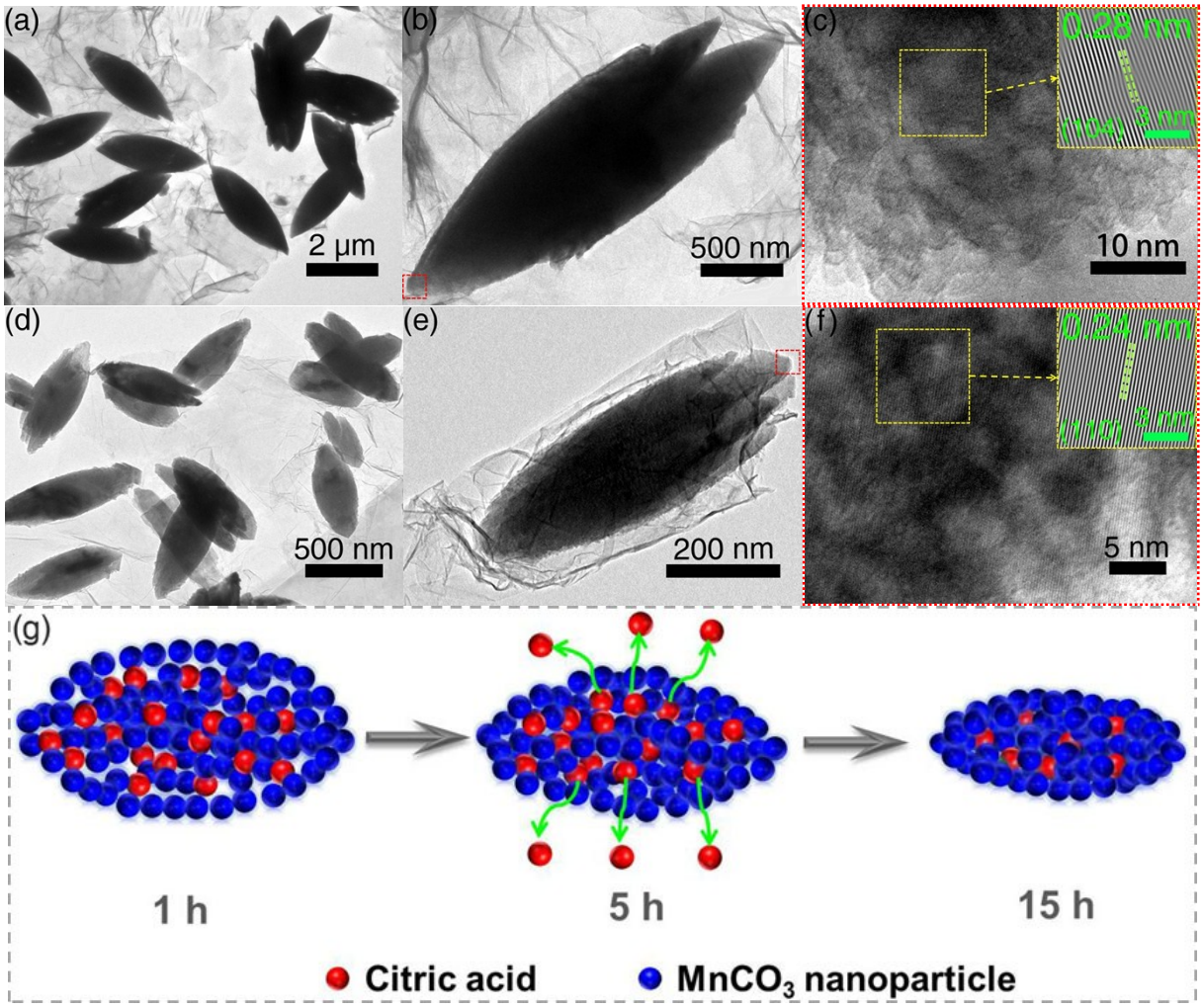

Fig. S3 TEM and HR TEM images of the intermediates collected from a hydrothermal crystallization system in the presence of GO at the incubation time of (a-c) 1 and (d-f) 10 h, respectively. (g) A schematic illustration of a $MnCO_3$ nanospindle for its time-dependent particle aggregation and simultaneous "extraction" of additive CA along with the extending incubation time.

The panels (a), (b), (d) and (e) of Fig. S3 indicate that $MnCO_3$ nanospindles may be sufficiently dispersed by the two-dimensional (2D) arrays of GO nanosheets, while the panels (c) and (f) present a high crystallinity for the spindle-shaped aggregates of $MnCO_3$.

By comparison, Fig.S3a, b, d and e show that the average size of $MnCO_3$ secondary nanospindles decreases along with the extending hydrothermal incubation time, which may be interpreted using the scheme shown in the panel (g) of Fig. S3.

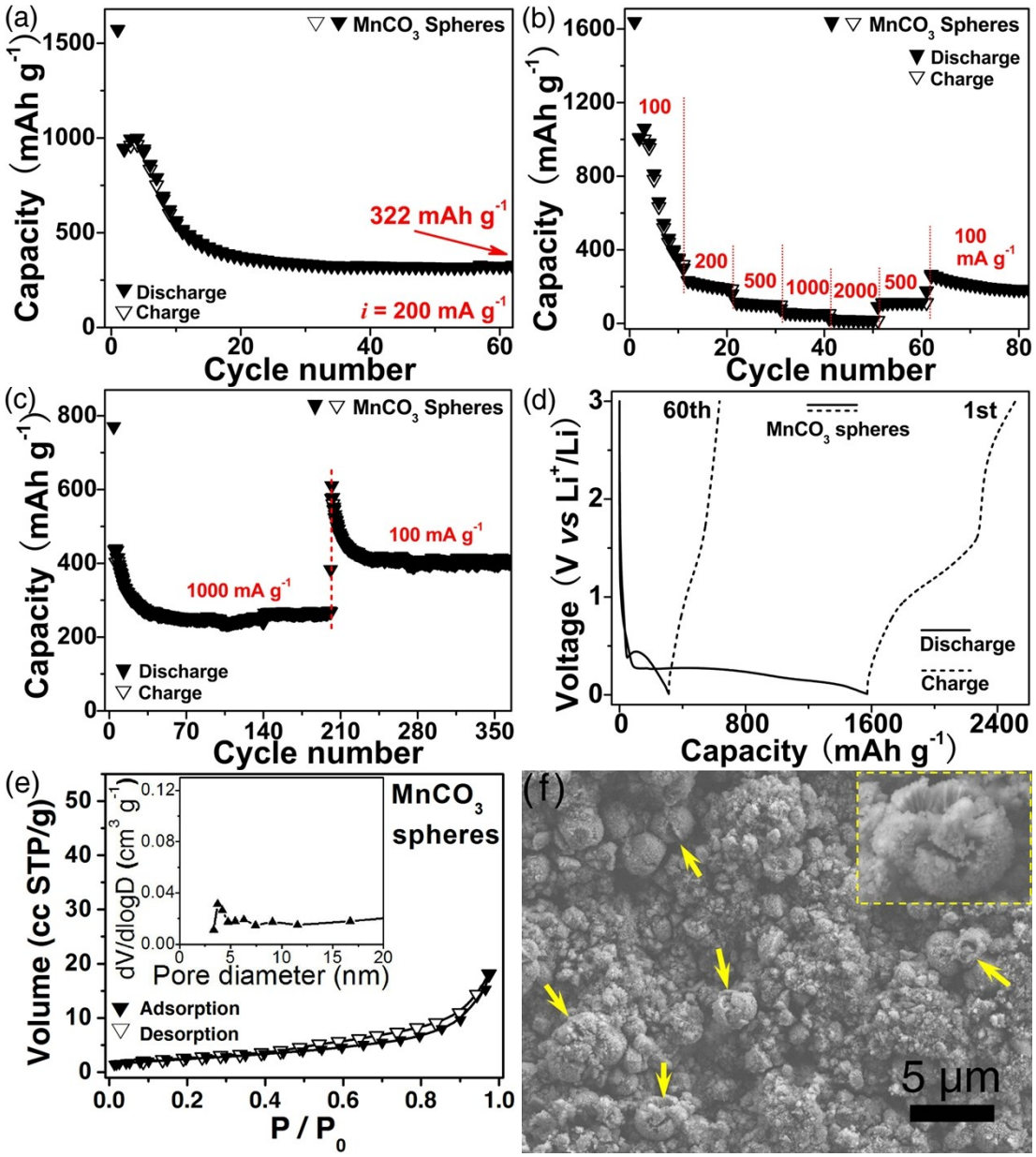

Fig. S4 (a, c) Cycling stabilities, (b) rate performance and (d) voltage profiles of $MnCO_3$ spheres operated at various C-rates. (e) N_2 adsorption-desorption isotherm of $MnCO_3$ spheres. (f) SEM image of the cycled $MnCO_3$ spheres operated at 200 mA g^{-1} after the 60th cycle.

In the absence of additives GO and CA, the resulting $MnCO_3$ spheres show the relatively bad lithium storage performances (Fig. S4a-d) comparing with those of $MnCO_3$ flowers and spindles-GO composites (Fig. 3a-d). Also by comparison, in the absence of CA the as-obtained $MnCO_3$ spheres acquire a slightly larger specific surface area (9 m^2 g^{-1}, Fig.S4-e) than that (4 m^2 g^{-1}) of $MnCO_3$ flowers sampled in the presence of CA (Fig.4b). As shown in panel (f) of Fig. S4, there is a relatively severe pulverization phenomenon for the cycled $MnCO_3$ spheres comparing with that of the cycled $MnCO_3$ flowers (Fig. 4d).

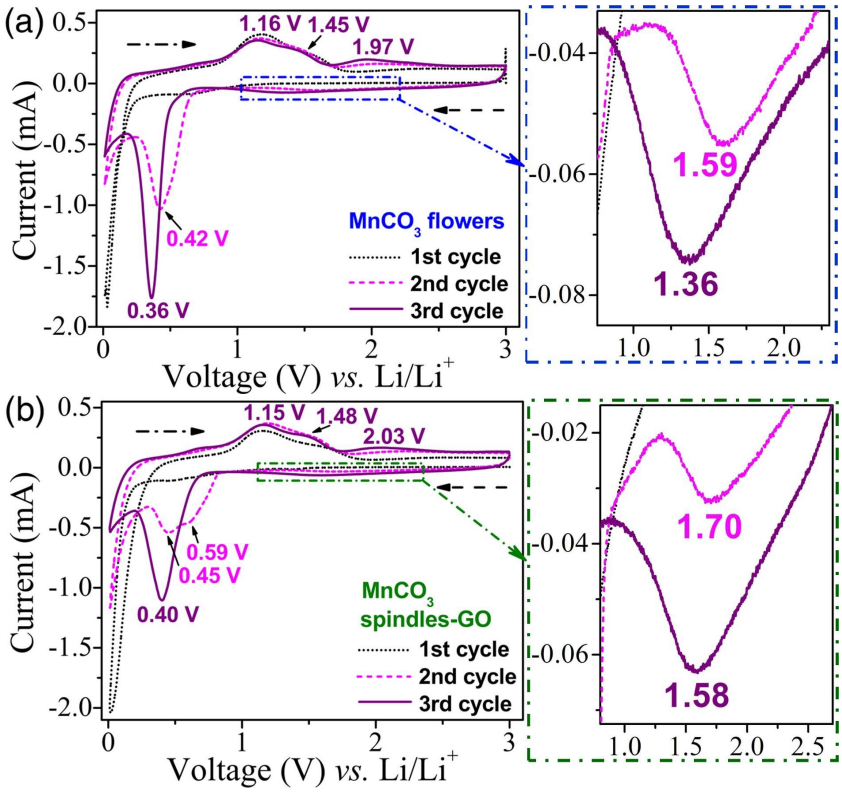

Fig. S5 Initial three CV curves of (a) $MnCO_3$ flowers and (b) $MnCO_3$ spindles-GO composites recorded at 0.1 mV s^{-1} within the potential range of 0.01-3.0 V *vs.* Li/Li^+.

Considering the "new" cathodic/anodic peaks at ~1.05/1.98 V in the 10th cycle (Fig. 4a), panel (a) or (b) of Fig. S5 also shows the gradually appearing cathodic/anodic peaks at ~1.36/1.97 V or at ~1.58/2.03 V. That is, this cathodic/anodic peak pair gradually emerges along with the increasing cycle number, which may correspond to the gradual electrochemical oxidation of Mn^{2+} to a higher valence (i.e. Mn^{3+}) as reported in literatures.

Generally, the potential difference between a pair of anodic-cathodic peaks could be used to qualitatively define the reversibility of a reversible electrochemical reaction, and the smaller the potential difference and the higher reversibility of the electrochemical reaction. According to these peak positions marked in the panel (a) of Fig. S5, the two peak potential differences of "pure" $MnCO_3$ are ca. 0.80 (= 1.16 - 0.36) V and 0.61 (= 1.97 - 1.36) V, respectively. According to these peak positions labbed in the panel (b) of Fig. S5, the two peak potential differences of GO-mixed $MnCO_3$ are ca. 0.75 (= 1.15 - 0.40) V and 0.45 (= 2.03 - 1.58) V, respectively. Therefore, the mixing of GO could cut down each peak potential difference, indicating that the effectively mixing of conductive GO could improve the electrochemical reversibility of anode active substance $MnCO_3$.

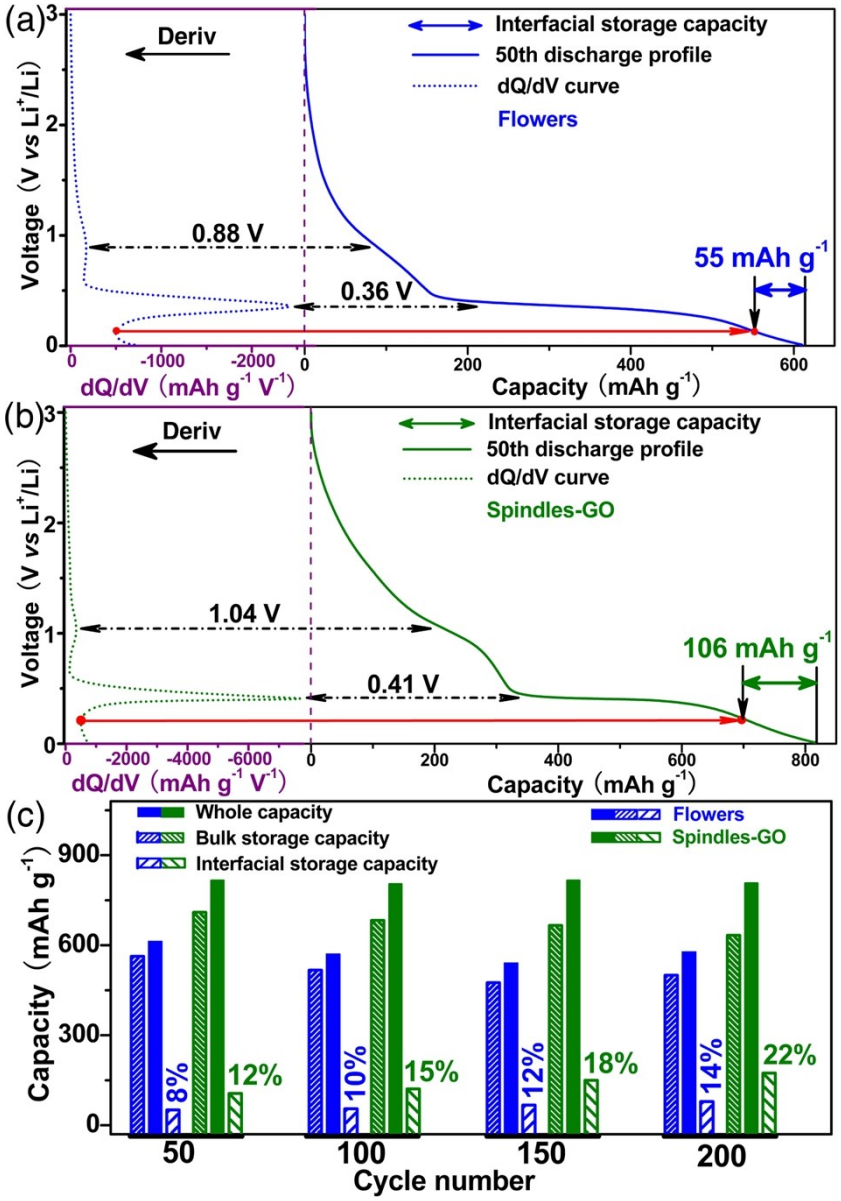

Fig. S6 (a, b) The combination of discharging profile and corresponding dQ/dV curve of $MnCO_3$ flowers and $MnCO_3$ spindles-GO composites operated at 1000 mA g^{-1} in the 50th cycle, respectively. (c) Histograms of the comparative interfacial storage capabilities of $MnCO_3$ flowers and $MnCO_3$ spindles-GO composites in each cycle.

As shown in Fig. S6a or 6b, the cathodic peaks of lithiation reaction in each dQ/dV curve correspond well with the voltage plateaus in the corresponding discharge profile. Also, the boundary between the bulk lithium storage (i.e., non-reactive and reactive storage) and interfacial lithium storage could be clearly determined by a horizontal red line therein. Furthermore, this boundary could be used to distinguish the interfacial Li-storage capacity from the whole capacity, marked in Fig. S6a and 6b and summarized in Fig. S6c.